Legendre *et al. Earth, Planets and Space* (2015) 67:28
DOI 10.1186/s40623-015-0193-3

Earth, Planets and Space
a SpringerOpen Journal

FULL PAPER Open Access

Anisotropic Rayleigh-wave phase velocities beneath northern Vietnam

Cédric P Legendre*, Li Zhao, Win-Gee Huang and Bor-Shouh Huang

Abstract

We explore the Rayleigh-wave phase-velocity structure beneath northern Vietnam over a broad period range of 5 to 250 s. We use the two-stations technique to derive the dispersion curves from the waveforms of 798 teleseismic events recoded by a set of 23 broadband seismic stations deployed in northern Vietnam. These dispersion curves are then inverted for both isotropic and azimuthally anisotropic Rayleigh-wave phase-velocity maps in the frequency range of 10 to 50 s. Main findings include a crustal expression of the Red River Shear Zone and the Song Ma Fault. Northern Vietnam displays a northeast/southwest dichotomy in the lithosphere with fast velocities beneath the South China Block and slow velocities beneath the Simao Block and between the Red River Fault and the Song Da Fault. The anisotropy in the region is relatively simple, with a high amplitude and fast directions parallel to the Red River Shear Zone in the western part. In the eastern part, the amplitudes are generally smaller and the fast axis displays more variations with periods.

Keywords: Seismic tomography; Surface waves and free oscillations; Wave propagation; Vietnam

Background

In the past few decades, the Himalayan mountain belt and the Tibetan Plateau have been extensively studied to understand the processes of collision between the Indian and Eurasian plates and the extrusion of the Tibetan Plateau (Avouac and Tapponnier 1993; Bird 2003; Tapponnier et al. 1986). The collision has resulted in a crustal thickening and associated uplift in and around the Tibetan Plateau. In the northern part of the South China Sea (Figure 1), several large sedimentary basins developed during the Cenozoic as a result of the extrusion of the Indo-China Block and the South China Block. This extrusion has an important impact on the tectonics of northern Vietnam (Tapponnier et al. 1986). This region is at the boundary between the South China Block and the Indo-China Block, with the Simao Block thought to be situated in between these two blocks, resulting in two major shear zones on its northern and southern boundaries (Figure 1).

The Red River Shear Zone (RRSZ) extends NW-SE for about 1,000 km from SE Tibet to the South China Sea (Avouac and Tapponnier 1993; Huang et al. 2009, 2013; Searle 2006; Tapponnier et al. 1986; Yeh et al. 2008). It is one of the major continental boundaries in Southeast Asia and separates the South China Block from the Indo-China Block. It is believed to have had a major impact on the tertiary tectonic evolution of Southeast Asia (Chung et al. 1997; Searle 2006; Wang et al. 2001). The RRSZ exhibits an extensive left-lateral motion with up to 900-km displacement in the past 30 Ma (Chung et al. 1997; Wang et al. 2001). It has been used as the prime example of a lithospheric-scale strike-slip fault that has accommodated hundreds of kilometers of the southeastward extrusion of the Indo-China Block away from the Indian Plate indentor (Avouac and Tapponnier 1993; Tapponnier et al. 1986).

The RRSZ splits into two strands of faults in northern Vietnam. The wider shearing system is suggested as a flower structure which might be developed with normal components in a transtensional stage of the RRSZ during 15 to 30 Ma, possibly related to the spreading of the South China Sea (Searle 2006; Yeh et al. 2008).

The timing of the RRSZ activity is constrained by geochronological data obtained predominantly from the Chinese portion of the shear zone. The major period of the RRSZ activity was determined by Chung et al. (1997) using geochronometers with a high-closure temperature. They point to the Oligo-Miocene, with an onset time of

*Correspondence: legendre@earth.sinica.edu.tw
Institute of Earth Sciences, Academia Sinica, 128 Academia Road, Sec. 2, Nangang, Taipei 11529, Taiwan

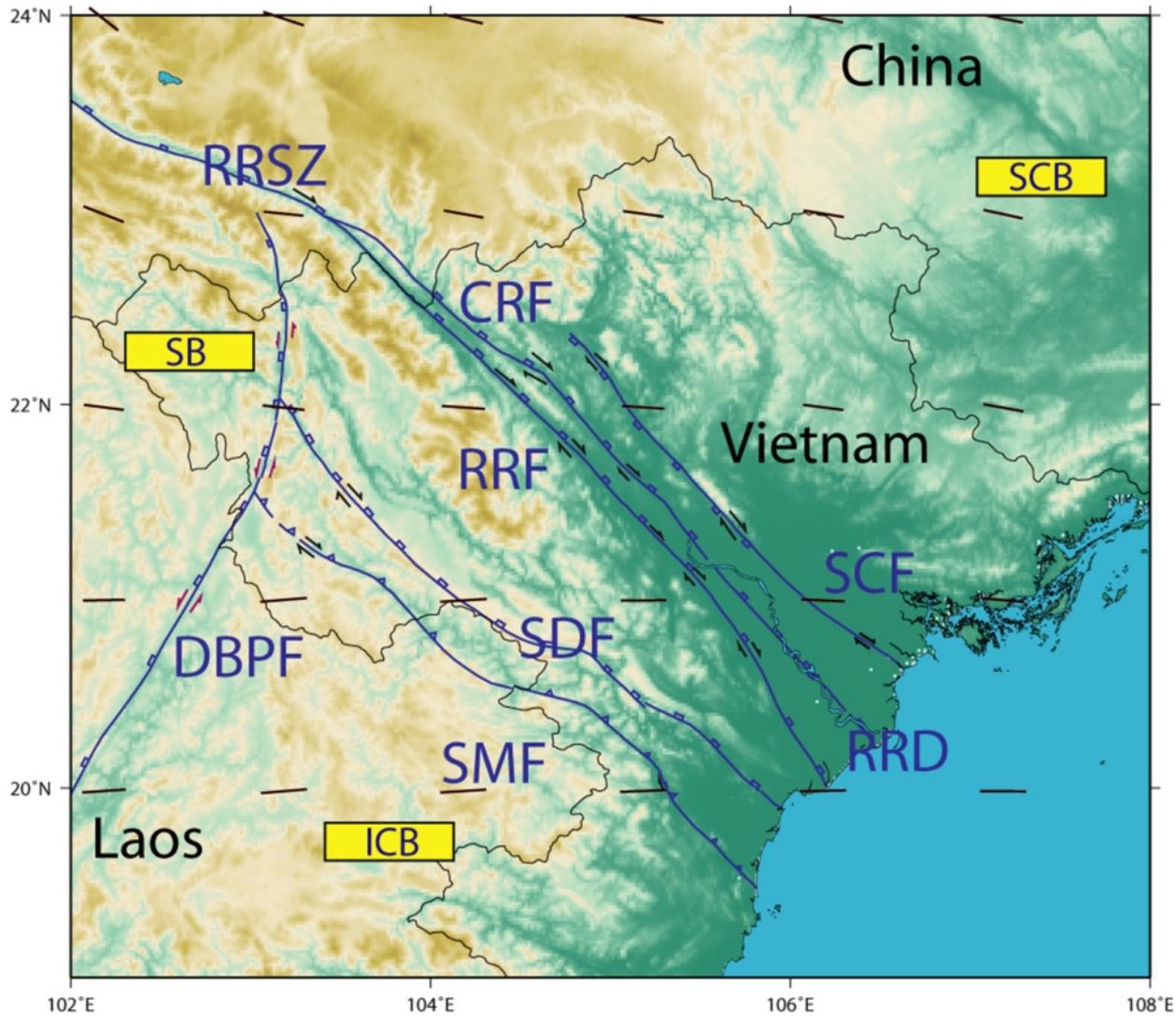

Figure 1 Tectonic map of the study area in northern Vietnam. Political boundaries and names of the countries are displayed in thin black lines. Three tectonic blocks (Indo-China Block - ICB; Simao Block - SB; and South China Block - SCB) are separated by several faults: the Red River Shear Zone (RRSZ), including the Chay River Fault (CRF), the Red River Fault (RRF) and the Song Chay Fault (SCF), the Dien Bien Phu Fault (DBPF), the Song Da Fault (SDF), and the Song Ma Fault (SMF). Short black lines correspond to the average plate motion in the region (Bird 2003).

21 to 27 Ma, after the beginning of India-Eurasia collision ca. 50 Ma (Avouac and Tapponnier 1993; Tapponnier et al. 1986).

The RRSZ is consistent with the continental extrusion model (Avouac and Tapponnier 1993; Tapponnier et al. 1986). Therefore, the RRSZ is commonly considered as a lithospheric suture separating the Indo-China Block from the South China Block. However, the RRSZ could also be an upper-crust structure that shears and exhumes the pre-existing metamorphic massif (Searle 2006). Like the RRSZ, the Dien Bien Phu Fault also has two phases of shearing, from dextral in the past to sinistral movement presently. The Dien Bien Phu Fault is therefore suspected to be a right-lateral conjugate fault system under the regional deformation in southeastern Asia (Huang et al. 2013). Chung et al. (1997) proposed that the Song Ma Fault may be a better candidate of the plate suture, and the RRSZ could be created by crustal weakening of the intraplate extension 30 to 40 Ma.

Seismic tomography provides a well-suited tool that can provide evidence to resolve those questions. However, northern Vietnam is a relatively poorly studied region seismologically, lacking in a variety of models for comparison (Huang et al. 2013; Pailoplee and Choowong 2014). New models providing observations at greater depths (asthenosphere and below) would be of great interest to investigate the effects of the influence of the deeper part of the RRSZ (Knapmeyer-Endrun et al. 2013).

Most of the previous tomographic models have been obtained from *P*-wave (Huang et al. 2013, 2009 Wang et al. 2003; Xu et al. 2005) and *S*-wave (Wang et al 2003) travel-time tomographies, as well as surface-wave analysis (Wu et al. 2004).

Using the *P*-wave travel-times from local earthquakes, Huang et al. (2002) imaged the crust and upper mantle structure under Yunnan, China. Their model exhibits a strong contrast between both sides of the RRSZ that could be imaged down to a depth of 85 km. Similar features are found in *S*-wave velocity models (Wang et al. 2003) and surface-wave results (Wu et al. 2004).

Using teleseismic earthquakes, Xu et al. (2005) found a high-velocity zone in the upper crust underlain by a low-velocity zone in the mid-lower crust along the RRSZ. But those models suffer from the lack of stations in northern Vietnam. They are either local studies focusing on the Yunnan province (Huang et al. 2002; Wang et al. 2003; Xu et al. 2005) or larger scale studies with a low resolution in northern Vietnam (Wu et al. 2004).

The first local seismic tomographic study of northern Vietnam became feasible when a portable broadband seismic network was installed in December of 2005 with the aim of imaging and interpreting crustal and mantle structures beneath northern Vietnam (Huang et al. 2009). In that study, datasets from the Vietnam Short-Period Seismic Network (VSPSN) and the Portable Broadband Seismic Network (PBSN) were combined in an attempt to improve the resolution of the three-dimensional (3D) crustal and uppermost mantle structure beneath northern Vietnam and the southeastern half of the RRSZ. They used crustal P, secondary crustal P, and Pn waves to invert for crustal and Pn velocities, as well as Moho depth variation. The results showed a segmentation of the RRSZ in the mid-lower crust, confirming the results of previous tomographic studies (Xu et al. 2005) beneath Yunnan province.

In this study, we will investigate the crustal and upper lithospheric mantle structure beneath northern Vietnam using interstation measurements of Rayleigh-wave phase velocities (Lebedev et al. 2006; Legendre et al. 2014, 2014a,b; Meier et al. 2004). We construct an anisotropic model of the Rayleigh-wave phase velocity using records at 23 broadband seismic stations from 798 teleseismic events.

Seismic stations and earthquakes

To measure the Rayleigh-wave phase velocities beneath northern Vietnam, we use the waveforms recorded at 23 broadband seismic stations from the PBSN in Vietnam (Huang et al. 2009). The stations, as shown in Figure 2, are more or less evenly distributed in our study region. We used the records at those 23 stations from 2005 to 2007.

In this study, we adopt the implementation of the cross-correlation approach of (Meier et al. 2004) to the two-station method. This method requires that the angle between the great circle connecting the given two stations and the great circle connecting this specific event to the station pair is small. In this study, we set an upper limit of 10° for this angle. Another condition is that the epicentral distance between the earthquake and the station pair is greater than the distance between the two stations. This ensures that the difference between the recorded waveforms at the two stations can be linked with the structure between the two stations. Epicentral distances are between 10° and 170°, and all interstation distances are in the range of 50 to 400 km.

Following these criteria, we extracted 31,513 records from 798 selected events (Figure 3). For each given pair of stations, all phase-velocity measurements obtained from different earthquakes are averaged to derive the dispersion curve for the path connecting this pair of stations. This resulted in reliable dispersion curves for a total of 229 interstation paths out of the 253 possible pairs of stations, as displayed in Figure 2.

Methods

The two-station method was first introduced by Sato 1955. It has been used to measure the dispersion curves of surface waves (Knopoff 1972). Meier et al. (2004) implemented the cross-correlation approach, which allows for the measurements of dispersion curves in a broad period range (in our case, between 5 and 250 s). We follow the conventional two-station approach in constructing the Rayleigh-wave phase-velocity maps in northern Vietnam. In the first step, we measure the phase-velocity using broadband regional waveform records (Figure 4) to determine the individual interstation dispersion curves for a specific path connecting two stations. In the second step, we invert the obtained collection of dispersion curves for regional Rayleigh-wave maps at selected periods.

For each selected event, the vertical-component displacements recorded at the two stations in each pair are cross-correlated (Figure 4). The cross-correlation is transferred into the frequency domain (Figure 5), and its complex phase $\zeta(\omega)$ is used to calculate the Rayleigh-wave phase velocity $C(\omega)$, as detailed in previous studies (Deschamps et al. 2008; Endrun et al. 2011; Lebedev et al. 2006; Legendre et al. 2014a; Meier et al. 2004). To minimize the effects of noise and interference, the cross-correlation function is first filtered with a frequency-dependent Gaussian band-pass filter (Meier et al. 2004). Side lobes caused by correlations of the fundamental mode with scattered waves and higher modes are then down-weighted by the application in the time domain of a frequency-dependent Gaussian window to the filtered cross-correlation function. This approach to filtering and windowing is effective as long as the fundamental mode

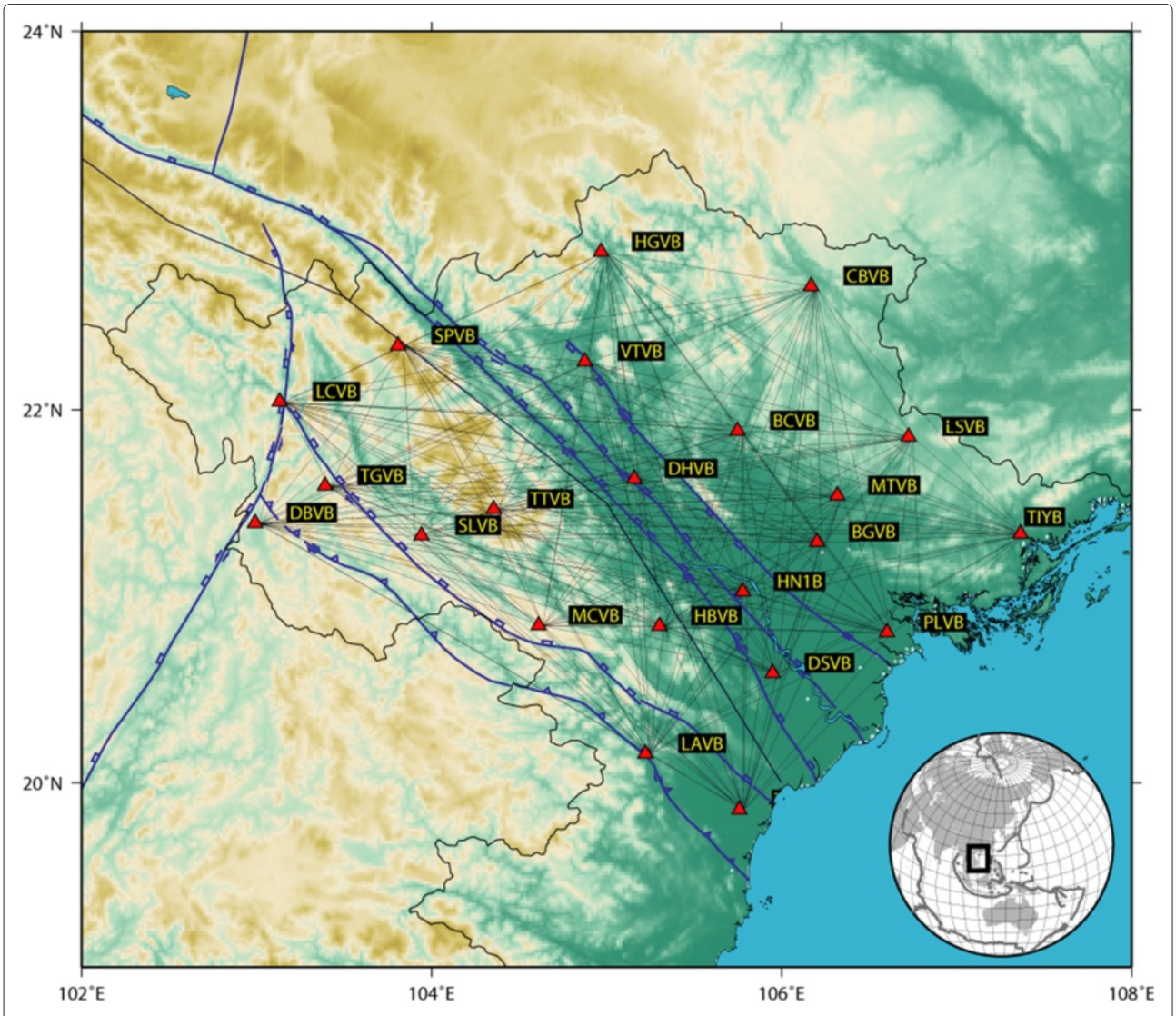

Figure 2 Seismic stations (red triangles) and possible interstation paths (black lines).

has the largest amplitude in the seismogram and therefore dominates the contribution to the cross-correlation function, which is always true at epicentral distances greater than 1,200 km (Endrun et al. 2011; Lebedev et al. 2006; Legendre et al. 2014a).

For each selected station pair, all measurements from available earthquakes (Figure 6 (top)) are averaged (Figure 6 (bottom)) to obtain a single path-specific dispersion curve. Averaged dispersion curves that are constrained by at least five single event-specific dispersion curves are kept for further analyses, and the rest are discarded.

From the 253 possible pairs of stations, we obtained a total of 229 phase-velocity dispersion curves for the fundamental Rayleigh-wave using the two-station method (Figure 7).

As the interstation distance is relatively small, measurements at long periods are less robust. Furthermore, we intend to focus on the crustal and upper lithospheric expression of the RRSZ; therefore, inversion of dispersion curves has been performed in the period range of 10 to 50 s only (Figure 8). This corresponds to the whole crust and uppermost lithospheric mantle.

After deriving the dispersion curves for the 229 interstation paths, we then invert them for both isotropic and anisotropic (2ψ and 4ψ) Rayleigh-wave phase-velocity maps at selected periods. At each point of the model, the total velocity anomaly can be parameterized with five coefficients: one coefficient for the isotropic phase-velocity variation, δC_{iso}; two coefficients for the 2ψ-anomaly, $A_{2\psi}$ and $B_{2\psi}$; and two coefficients for the

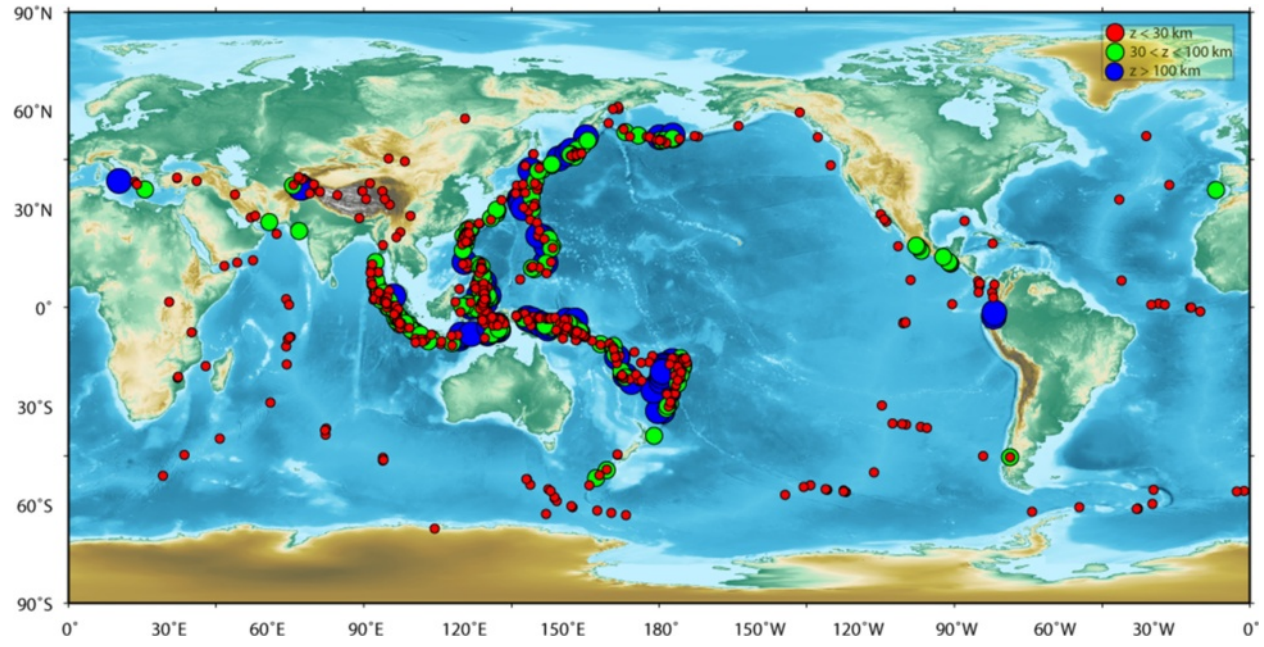

Figure 3 Events used for the measurement of interstation dispersion curves. Circles represent the locations of the epicenters, and the colors indicate the depths of the events (red: 0 to 30 km; green: 30 to 100 km; blue: 100+ km). The sizes of the circles are proportional to the event magnitudes.

4ψ-anomaly, $A_{4\psi}$ and $B_{4\psi}$ (Deschamps et al. 2008; Endrun et al. 2011):

$$\begin{aligned}\delta C = \delta C_{\text{iso}} &+ A_{2\psi}\cos(2\psi) + B_{2\psi}\sin(2\psi) \\ &+ A_{4\psi}\cos(4\psi) + B_{4\psi}\sin(4\psi).\end{aligned} \tag{1}$$

The amplitudes of azimuthal velocity variation (Λ) and the directions of fast propagation (Θ) of the 2ψ- and 4ψ-anisotropy are then given by:

$$\begin{cases}\Lambda_{2\psi} = \sqrt{A_{2\psi}^2 + B_{2\psi}^2} \\ \Theta_{2\psi} = \frac{1}{2}\ \arctan\left(\frac{B_{2\psi}}{A_{2\psi}}\right)\end{cases} \quad \text{and} \quad \begin{cases}\Lambda_{4\psi} = \sqrt{A_{4\psi}^2 + B_{4\psi}^2} \\ \Theta_{4\psi} = \frac{1}{4}\ \arctan\left(\frac{B_{4\psi}}{A_{4\psi}}\right).\end{cases} \tag{2}$$

Each dispersion curve yields the average phase velocity along the path linking the two stations as a function of period, and the total average phase-velocity anomaly along the path may be written as the integral of local anomalies at each grid knot sampled by the given path:

$$\delta\bar{C}_i = \int_\varphi \int_\theta K_i(\varphi,\theta)\ \delta C(\varphi,\theta)\ d\theta\ d\varphi\ , \tag{3}$$

where the local anomalies $\delta C(\varphi,\theta)$ are weighted by the sensitivity kernels $K_i(\varphi,\theta)$. The kernel provides the contribution at each knot on a specific path to the total phase-velocity anomaly (Deschamps et al. 2008; Lebedev and Van Der Hilst 2008).

The sensitivity kernels $K_i(\varphi,\theta)$ are evaluated at a global triangular grid of knots with an approximately equal interknot spacing of, on average, 5 km (Lebedev and Van Der Hilst 2008; Lebedev et al. 2006; Wang and Dahlen 1995). For every knot, we identify the pentagons or hexagons around it that contain all points that are closer to this than any other knot. We compute the areas of the hexagons (or pentagons) around the knots. $K_i(\varphi,\theta)$ are calculated at each knot and multiplied by the area of the hexagon (or pentagon) around to yield the weight of the knot in the integral over the sensitivity area.

We also define a model grid, with interknot spacing of 20 km following Wang and Dahlen (1995). Rayleigh-wave phase-velocity perturbations at the locations of these knots are the unknowns in the inversion.

The kernels $K_i(\varphi,\theta)$ are evaluated at the model grid knots by integrating over the neighboring integration-grid knots.

The generalized matrix is composed of five submatrices:

$$G = G_{\text{iso}} + G_{C2\Psi} + G_{S2\Psi} + G_{C4\Psi} + G_{S4\Psi} \tag{4}$$

with:

$$G_{\text{iso}} = \begin{bmatrix} K_{11} & \dots & K_{1M} \\ \dots & \dots & \dots \\ K_{N1} & \dots & K_{NM} \end{bmatrix} \tag{5}$$

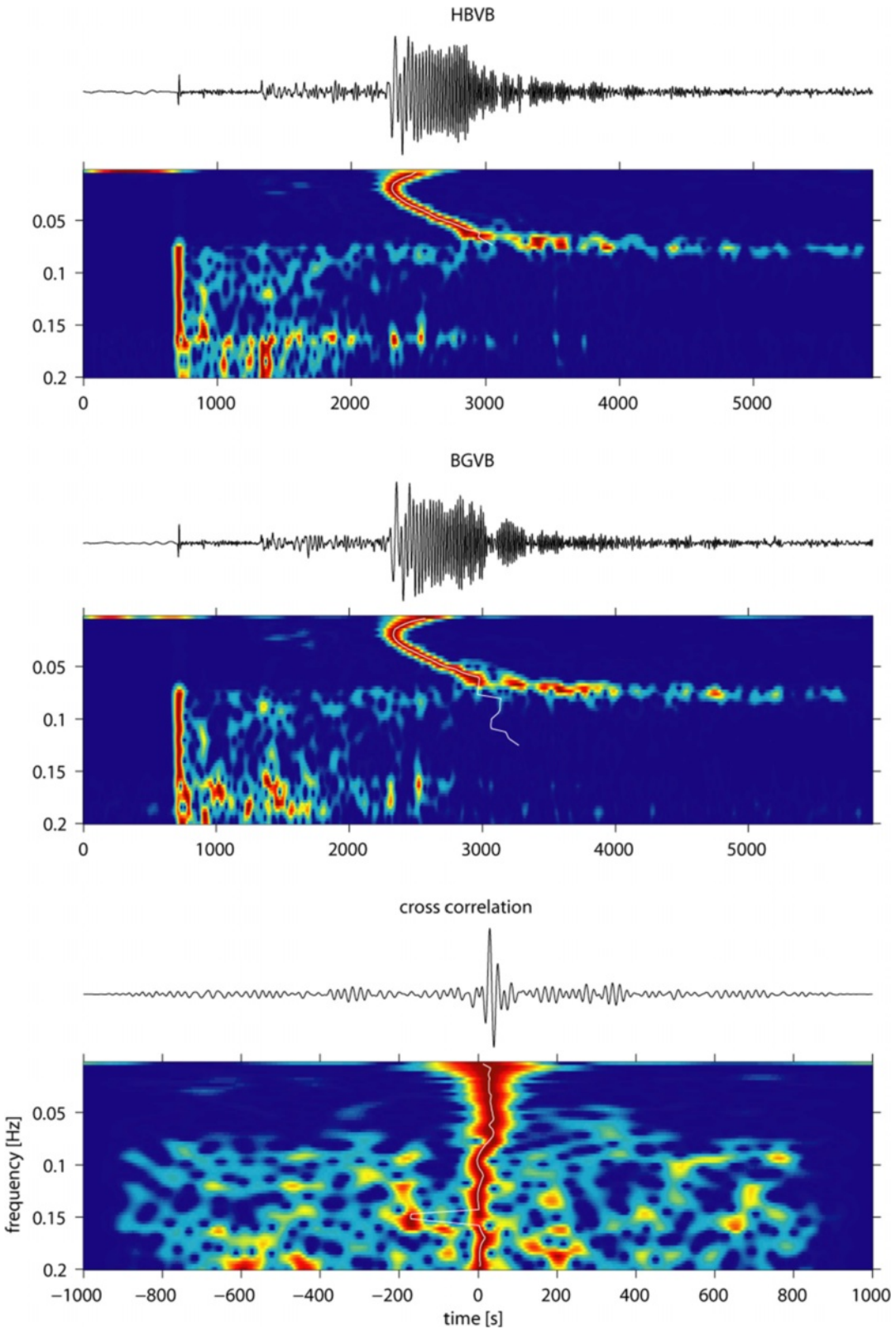

Figure 4 Seismograms and corresponding spectro-temporal diagrams for an event occurring in Indonesia in July 2007, and recorded at stations HBVB (top) and BGVB (bottom). The bottom panel shows the cross-correlation between the two seismograms and the corresponding spectro-temporal diagram. The white curves represent the maximum energy recorded for all frequencies.

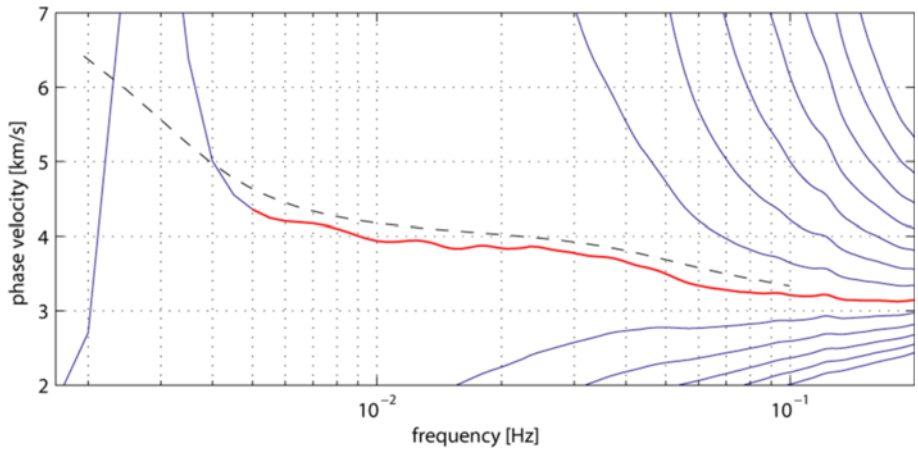

Figure 5 Measurements of an individual Rayleigh-wave dispersion curve obtained for a specific station pair from a single event. Possible dispersion curves from the inversion (solid blue lines), selected curve (red line), and dispersion curve for the reference model (dashed line).

$$G_{C2\Psi} = \begin{bmatrix} a_1K_{11} & \dots & a_1K_{1M} \\ \dots & \dots & \dots \\ a_NK_{N1} & \dots & a_NK_{NM} \end{bmatrix}, G_{S2\Psi} = \begin{bmatrix} b_1K_{11} & \dots & b_1K_{1M} \\ \dots & \dots & \dots \\ b_NK_{N1} & \dots & b_NK_{NM} \end{bmatrix},$$

$$G_{C4\Psi} = \begin{bmatrix} c_1K_{11} & \dots & c_1K_{1M} \\ \dots & \dots & \dots \\ c_NK_{N1} & \dots & c_NK_{NM} \end{bmatrix}, G_{S4\Psi} = \begin{bmatrix} d_1K_{11} & \dots & d_1K_{1M} \\ \dots & \dots & \dots \\ d_NK_{N1} & \dots & d_NK_{NM} \end{bmatrix}.$$

In these matrices, the K_{ij} are the weights of path i for knot j of the sensitivity areas, and the azimuthal dependence is accounted for by the constants $a_i = \cos(2\Psi_i)$, $b_i = \sin(2\Psi_i)$, $c_i = \cos(4\Psi_i)$, and $d_i = \sin(4\Psi_i)$, where Ψ_i is the azimuth of the path i.

The phase velocities obtained from the dispersion curves are averaged for each period, and the inversion is performed to obtain the phase-velocity perturbations relative to the regional average model by a damped, smoothed LSQR. We then solve this system using the LSQR method (Paige and Saunders 1982) with lateral smoothing and slight norm damping. Isotropic and anisotropic terms are smoothed and damped independently.

Resolution tests

In the following, we will show the resolution tests we conducted on the regularization parameters chosen for the final inversion, and the effect of these parameters on the resulting models. The regularization parameters include norm damping and smoothing. The norm damping is used to constrain the amplitudes of phase-velocity perturbations during the inversion. Therefore, investigations on this parameter allow us to calibrate our inversion.

As shown in Figure 9a,b,c,d,e for inversion tests using dispersion curves at 40 s, the norm-damping isotropic constraint does not affect the lateral distribution of the anomalies or the anisotropic part. Increasing norm damping only decreases the amplitude of the velocity anomaly. Therefore, this parameter has been set based on the standard deviation of the observed dispersion curves (Figure 7), from which the maximum amplitude of the anomalies can be estimated. Similar tests have been performed with the anisotropic part, in order to have realistic amplitudes for the anisotropy.

Lateral smoothing penalizes the difference between the anomaly at a knot and the average of the anomalies at its neighboring knots by minimizing the first and second spatial derivatives of velocity anomalies (Lebedev and Van Der Hilst 2008; Lebedev et al. 2006; Wang and Dahlen 1995). The lateral smoothing weight is chosen independently for each period. The strength of the lateral smoothing varies from one period to another, so as not to oversmooth excessively. We apply a stronger smoothing with decreasing path coverage. Figure 9f,g,h,i,j demonstrates the effect of smoothing on the resulting velocity model at a period of 40 s. With increased smoothing, the small-scale anomalies vanish, but if the smoothing is too high, we might lose actual resolution on the structures. Note that smoothing the isotropic component does not affect the anisotropic part, indicating the robustness of our inversion.

As shown in Figure 9k,l,m,n,o, the anisotropic smoothing parameters chosen for the inversion have an important effect on the resulting anisotropic models. If the smoothing on the anisotropic component is too small, the resulting models could display a high variability of the anisotropy both laterally and vertically (with period). If this parameter is too large, the only information that can be extracted from the model is the average direction of the anisotropy in the region.

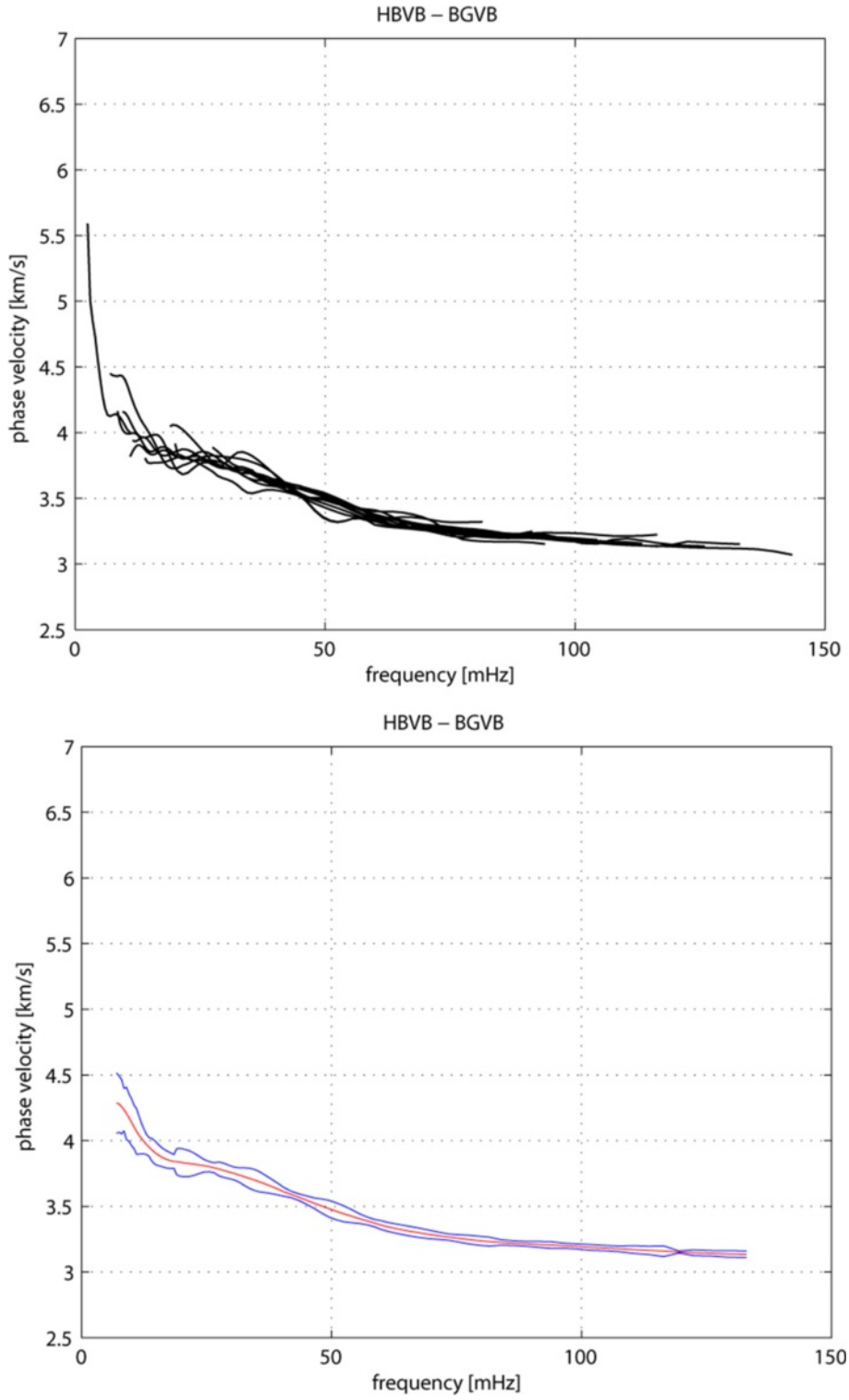

Figure 6 Individual dispersion curves and the resulting averaged dispersion curve. Individual dispersion curves measured for a specific station pair from all events (top) and the resulting averaged dispersion curve (bottom). Blue curves are for one standard deviation.

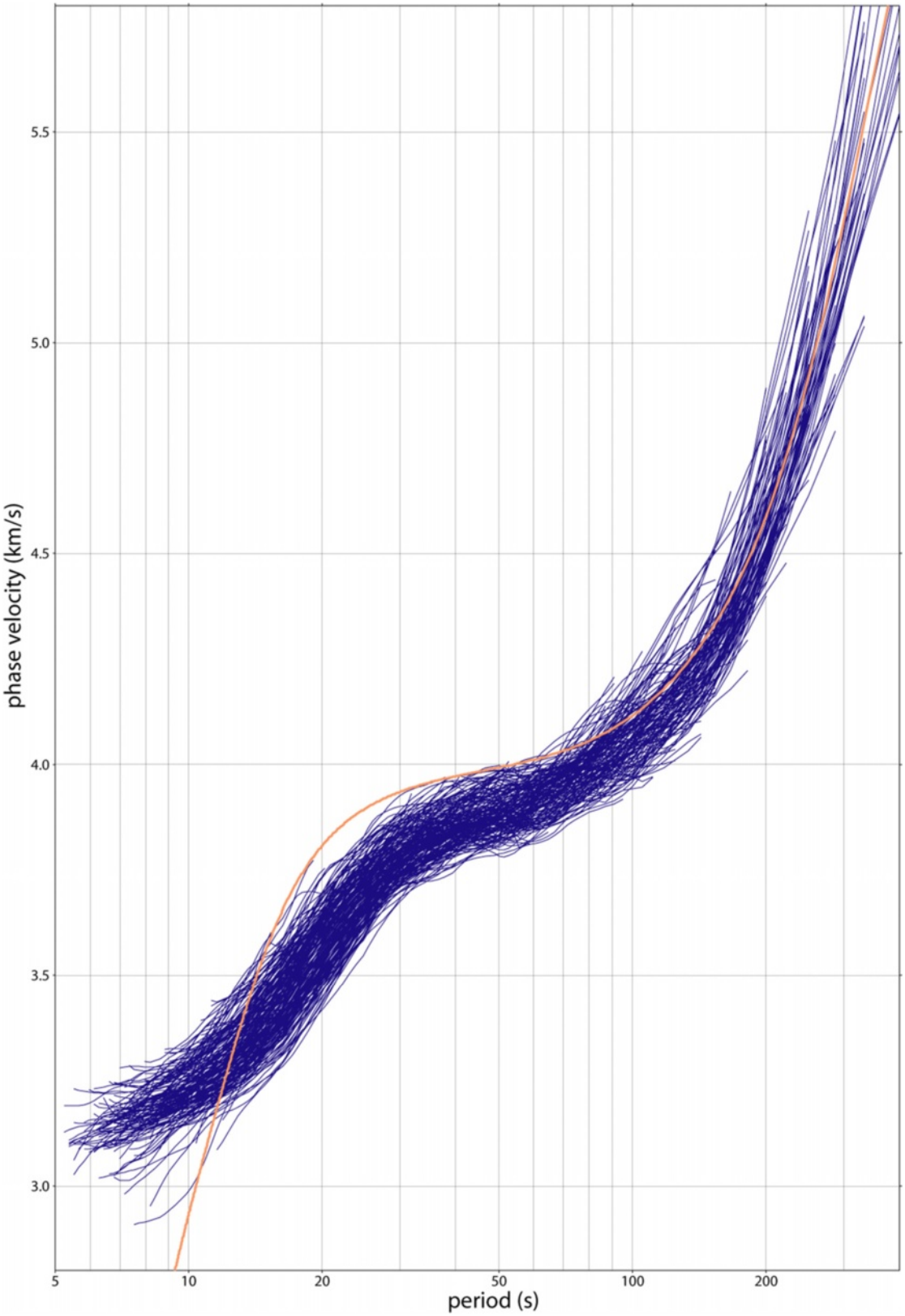

Figure 7 All dispersion curves selected for the inversion of the Rayleigh-wave phase velocity in this study. The orange line is the predicted phase velocity calculated from a 1D reference Earth model AK135 (Kennett et al. 1995).

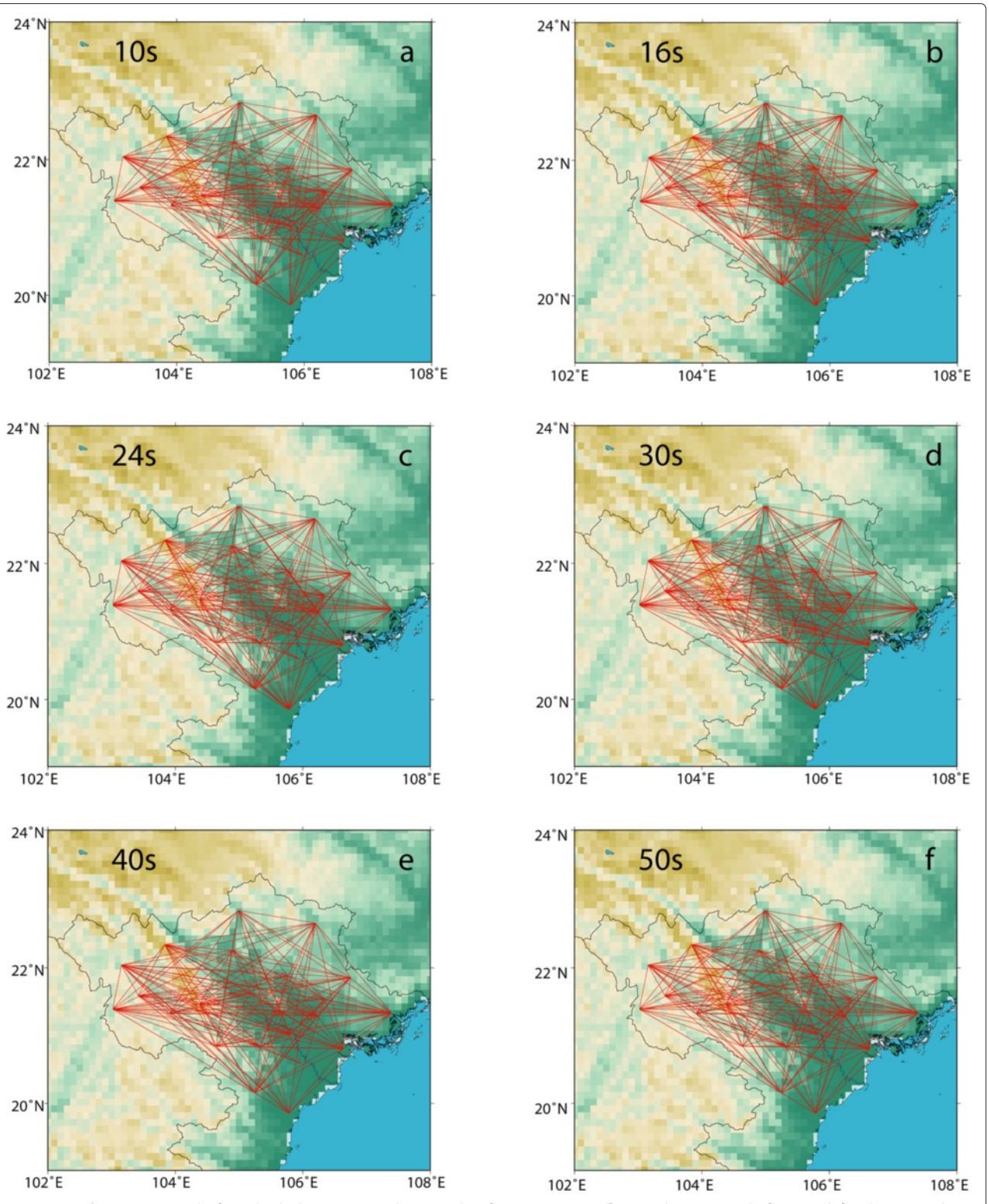

Figure 8 Path coverage. Paths for individual interstations that provide information at specific periods, respectively, from top left to bottom right: 10 s **(a)**, 16 s **(b)**, 24 s **(c)**, 30 s **(d)**, 40 s **(e)**, and 50 s **(f)**.

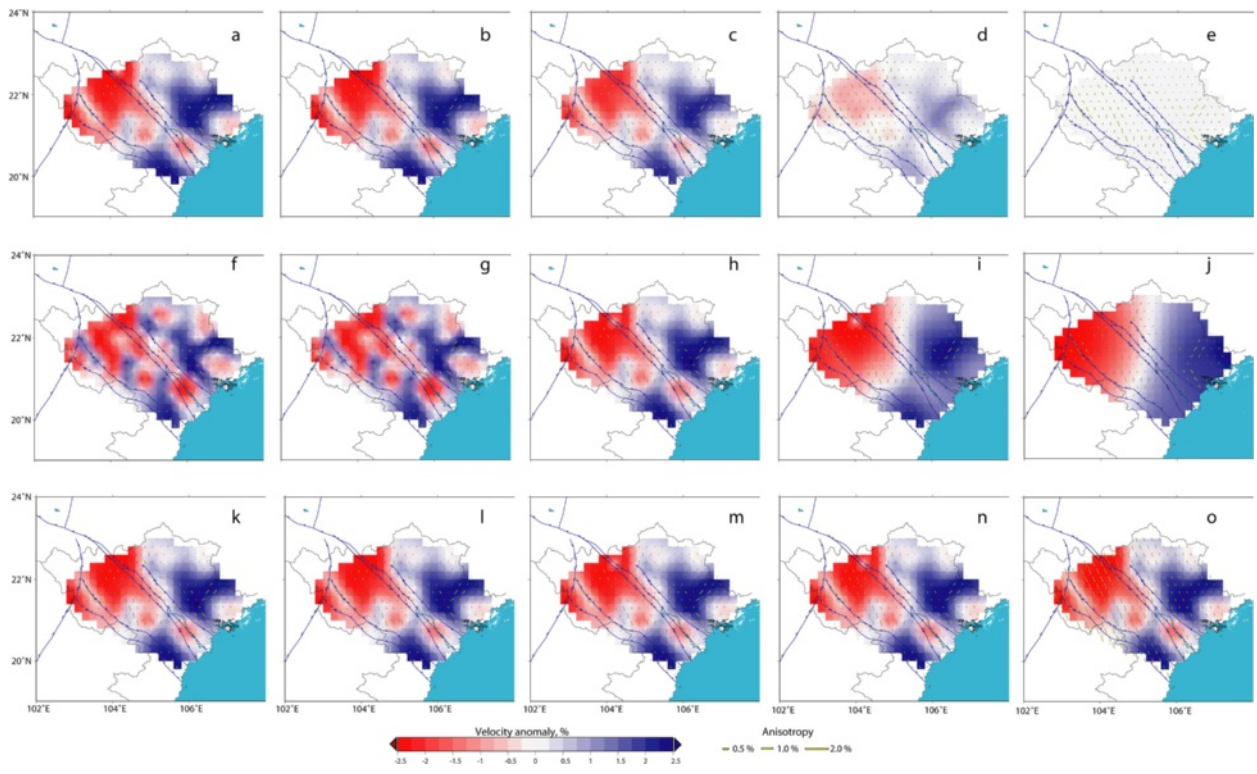

Figure 9 Models obtained with various values for a given period of 40 s. Models obtained with various values of the isotropic norm-damping **(a, b, c, d, e)**, isotropic smoothing **(f, g, h, i, j)**, and smoothing of the anisotropic penalization **(k, l, m, n, o)** for a given period of 40 s. Images from the left to the right are calculated with increasing values of the parameters. The preferred values chosen for the final inversion can be found in pannels **(c)**, **(h)**, and **(m)**.

Our preferred model (Figure 9c,h,m) is defined by a compromise between model smoothness (which is chosen to be as small as possible) and the ability to explain the observed data (variance reduction).

To test the robustness of the structures imaged by our models, we also performed a series of synthetic tests (Figure 10). We create a series of synthetic models with various isotropic and anisotropic patterns. First, we assume a synthetic model and expand it on the grid used in the inversion of real data and multiply this model vector with the kernel matrix. This results in a synthetic data vector, which is inverted using the same regularization scheme as that used for the inversion of the real data. In particular, the same amount of smoothing and damping and the same path coverage are used for a given period. This allows testing for the reconstruction of both anomalies and anisotropic patterns. The retrieval of the anomalies should display correct amplitudes and locations. The anisotropic features should be retrieved with consistent directions and amplitudes. Previous studies (Montagner and Tanimoto 1991; Trampert and Woodhouse 2003) have pointed out that the contribution of 4ψ terms may be non-negligible, which is why we have included them in our inversions. However, Deschamps et al. (2008) found that although the 4ψ terms have amplitudes comparable to those of the 2ψ terms, they are not needed to explain the raw data. Therefore, in discussing inversion results in this study, we will not attempt to interpret the 4ψ terms and focus only on the isotropic and 2ψ anisotropic anomalies. At all periods (from 10 to 50 s) tested, the retrieval of the synthetic model was sufficient, with no obvious artifacts in either isotropic and anisotropic perturbations (Figure 10).

Results and discussions

We obtained variations in Rayleigh-wave phase-velocity anomalies both with location and period (Figure 11). Because the Rayleigh wave of different periods sample different depth layers, the variations of Rayleigh-wave phase velocity with period are related to vertical variations in velocity anomalies. Our models are discussed in term of periods, which can be related to depth by means of phase-velocity sensitivity kernels (Huang et al. 2013; Legendre et al. 2012; Wang et al. 2003; Xu et al. 2005) as displayed Figure 12.

The obtained Rayleigh-wave phase-velocity maps are plotted in Figure 11. In the shallower part of the model, several small-scale anomalies can be found. For example,

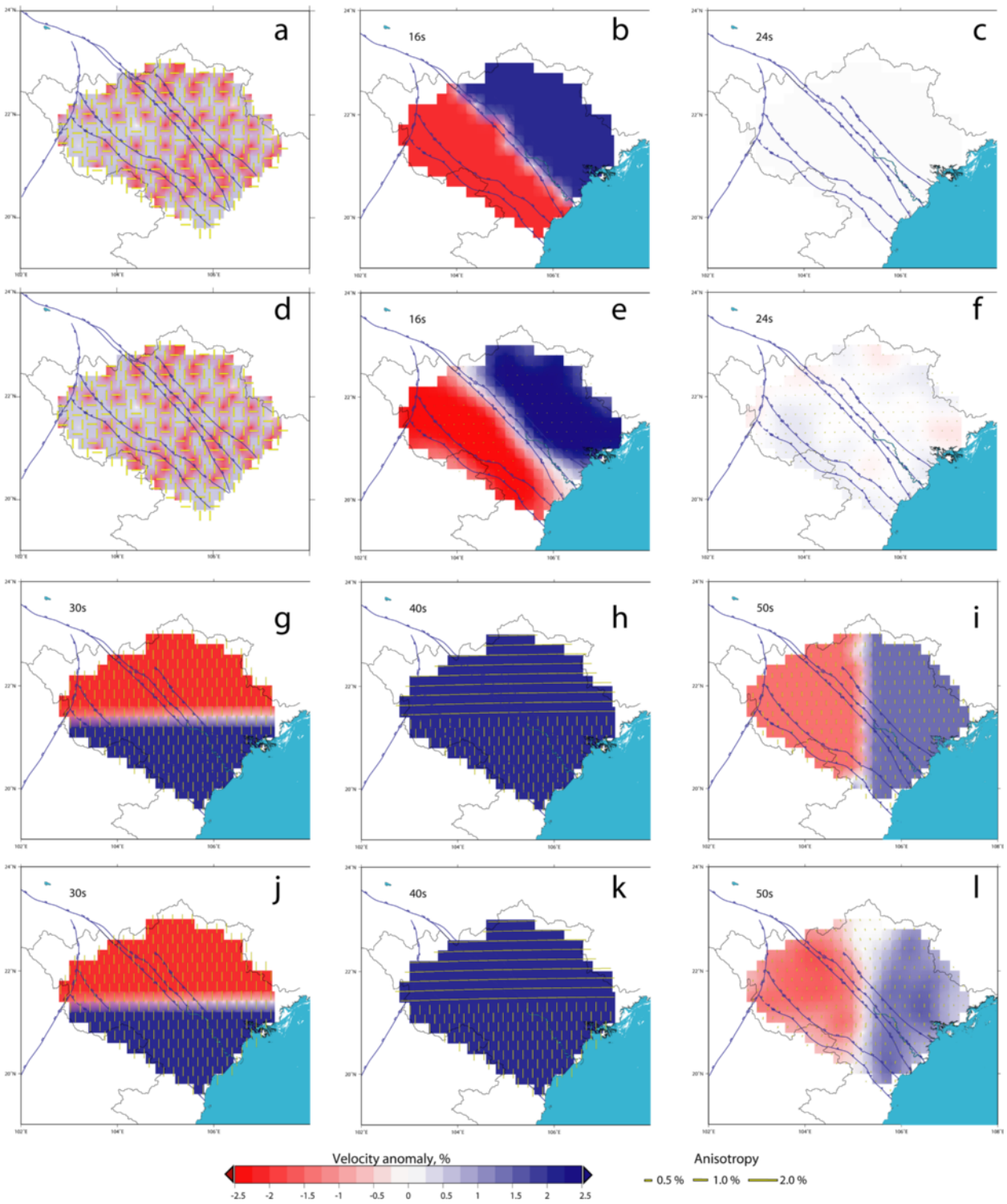

Figure 10 Resolution tests. Test models at periods of 10 s **(a)**, 16 s **(b)**, 24 s **(c)**, 30 s **(g)**, 40 s **(h)**, and 50 s **(i)** and reconstructed models **(d, e, f, j, k, l)** for respective periods. The reconstructions are performed to test the retrieval of both isotropic and anisotropic structures.

at the periods of 10 and 16 s, sampling the crust, the main pattern is the several NW/SE bands, parallel to the RRSZ.

At the period of 24 s, sampling the crust and lithosphere, the pattern evolves with the emergence of a slow-velocity area in the NW. The phase velocity beneath this

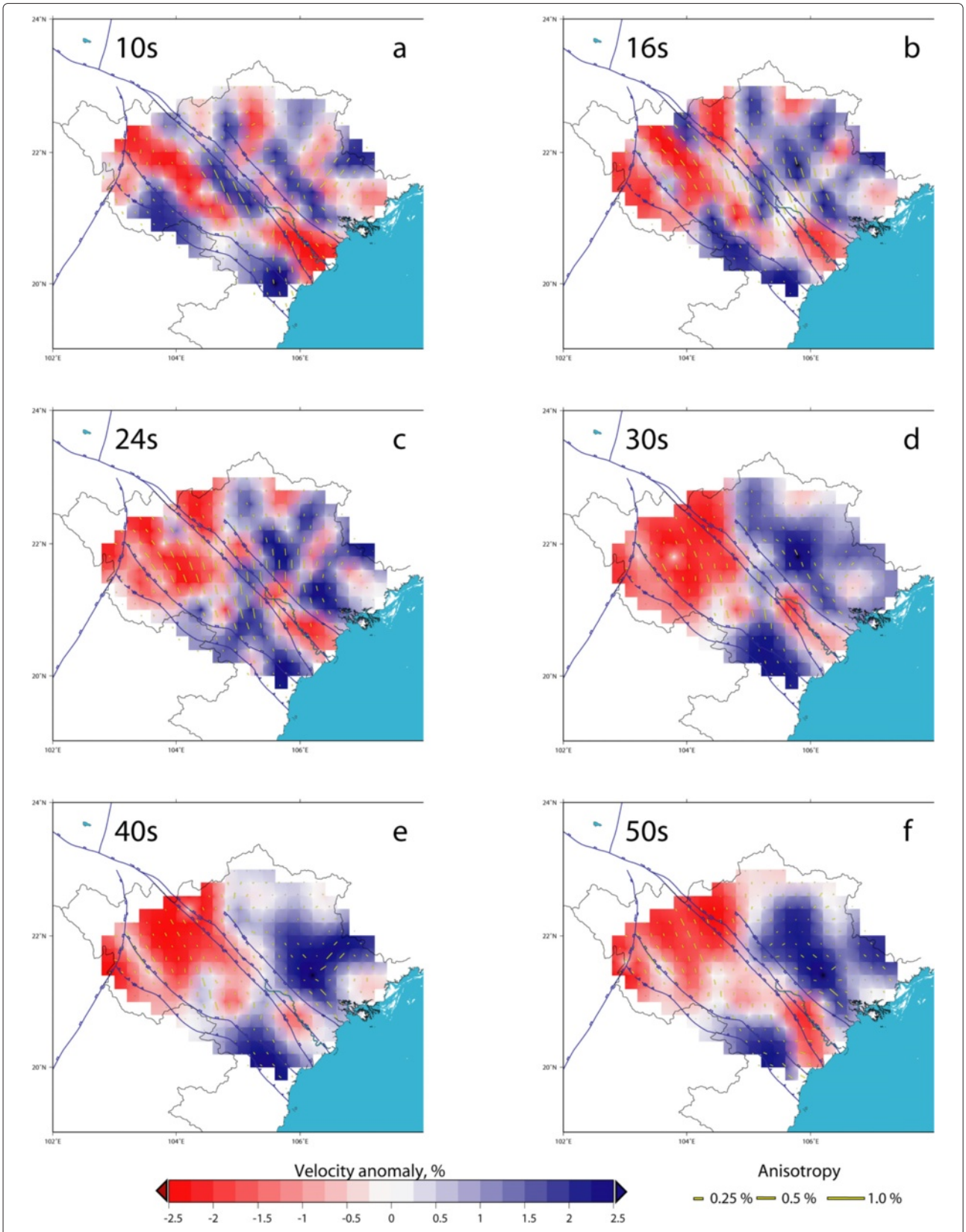

Figure 11 Isotropic and azimuthally anisotropic phase-velocity maps for northern Vietnam at specific periods. From top-left to bottom-right 10 s **(a)**, 16 s **(b)**, 24 s **(c)**, 30 s **(d)**, 40 s **(e)** and 50 s **(f)**.

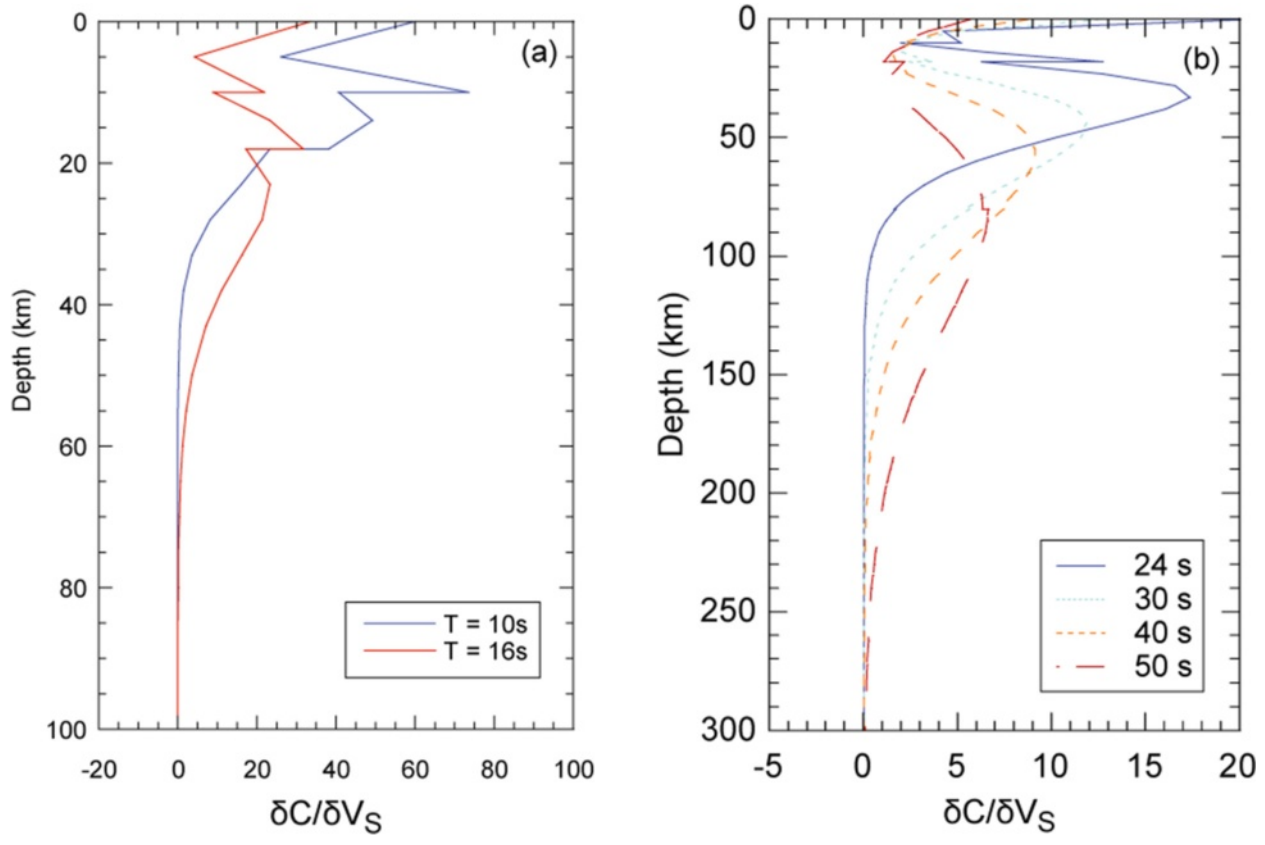

Figure 12 Sensitivity of the Rayleigh-wave phase velocity in function of depth for selected periods. (a) Sensitivities for 10 and 16 s. **(b)** Sensitivities for 24, 30, 40, and 50 s.

region remains stable at longer periods. At periods of 30 s and longer, sampling the lithosphere, the structure seems smoother, with less small-scale variations in phase velocity.

Fault systems

The models at shorter periods sample the crust and display high-velocity lineaments (Figure 11a,b). We can compare the models to the surface expression of the faults.

At 10 s (Figure 11a), a NW/SE slow-velocity band can be found beneath the Song Ma Fault and beneath the Chay River Fault (20.5°N, 106°E - Figure 1). The slow velocity in those regions could be induced by an intense deformation and faulting (breaking the rocks and therefore reducing the velocity) and the presence of fluids (Searle 2006). In the shallowest part of the model, at a period of 10 s (Figure 11a), the anisotropy between the RRSZ and Song Ma Fault is nearly parallel to the faulting, whereas the anisotropy in the western part of the model is almost perpendicular to the RRSZ. However, at periods of 16 s, the fast directions of the anisotropy are almost parallel to the RRSZ (Figure 11b) in the western part of the model. The western boundary of the RRSZ displays generally higher amplitudes for the anisotropy. The boundaries are not obvious with velocity perturbations only, but the anisotropic pattern is an additional constraint that can help to unravel the shape of the tectonic units.

A study of peak ground motion attenuation (Nguyen et al. 2012) for northern Vietnam based on shallow local earthquakes provided ground acceleration and peak ground velocity maps for the shallow surface. The general shape of the boundaries between the high and low velocities they present provides structural and geological details that are also in good agreement with our observations at shorter periods. Their map of peak ground acceleration and velocity show very low velocities in the northwestern part of the model and fast velocities in the eastern part. Those maps are very smooth but in agreement with the location of the boundaries deduced from both the isotropic and anisotropic part of our model at short periods.

The velocities beneath the Red River delta are lower than the surrounding region for all periods. However, at 10 and 16 s, the lowest velocities are found beneath the Song Ma Fault. This confirms recent analyses of structural

fabrics in a metamorphic complex located beneath the Chay River Fault and suggests that the Song Ma is purely an upper-crust structure that shears and exhumes the pre-existing metamorphic massif (Searle 2006; Yeh et al. 2008), and the RRSZ could be a lower-crust structure, in agreement with a previous tomographic study in the region (Huang et al. 2013). At intermediate periods (16 to 40 s), a zone of high velocities cuts across the RRSZ. This anomaly has already been observed in previous local tomographic studies (Huang et al. 2013) and is related to the geology of the region.

Chung et al. (1997) proposed that the Song Ma Fault is a better candidate of the plate suture, but our model suggests a transition region between the Song Da and Red River Fault (Figure 1). Between the Red River Fault and Song Da Fault, slow velocities are found (down to −2%) at short periods (10 to 30 s). Between those faults, the slow velocities might originate from intense deformation, faulting, or the presence of fluids. Beneath the fault regions, a more stable unit is found. This unit appears to be a less deformed region (weaker anisotropy) surrounded by faults, and the faster velocities can be related to the granitic composition of this block. The blocks (South China Block and Indo-China Block) surrounding those two faults (Red River Fault and Song Da Fault) also display faster velocities at crustal depths (10 to 24 s). The high velocities beneath the Indo-China Block and the SW-NE dichotomy in the isotropic structure (10 to 16 s) may originate from two combined effects. Both blocks belong to different units: RRSZ exhibits 500 to 900 km in extensive left-lateral displacement (Chung et al. 1997; Wang et al. 2001). The structure of both blocks is quite different, with volcanoes in the Yunnan and Simao Block regions (Huang et al. 2002) and a cratonic block (South China Block) in the northeast.

At periods of 10 and 16 s, a high-velocity belt is found (22.5°N, 104°E). This feature disappears in the lower crust (24 s) and becomes a low-velocity belt, which is well consistent with the models of Xu et al. (2005) and Lei et al. (2009) in Yunnan Province. Huang et al. (2013) interpreted this velocity anomaly in terms of metamorphic batholith at the surface with a possible melt at greater depths.

Crustal thickness

The average distribution of velocity perturbations at a period longer than 24 s, sampling both the crust and upper lithosphere, indicates an E/W dichotomy, with slow velocities in the west and faster velocities in the eastern part of the model. This could indicate a thickening of the crust towards the northwest, in agreement with previous receiver function analyses in northern Vietnam: Nguyen et al. (2013) used teleseismic converted waves to constrain the crustal structure of northern Vietnam. Their Moho map also display a north-south dichotomy, with a Moho depth around 25 km in the southern part and 35 km in the northern part. This is also in good agreement with our velocity maps for periods longer than 24 s.

At crustal depths, anisotropy is almost constant in the models: the fast direction of anisotropy is close to being parallel to the orientation of the RRSZ (NW/SE) in the SW, whereas the NE of the model does not display significant anisotropy. This could indicate that the blocks have been shifted with low deformation, accommodated by the RRSZ and the Indo-China Block.

Despite the fact that two different techniques and datasets have been used, the *P*-wave tomography (Huang et al. 2013) focused on the upper 30 km displays a good correlation with our model at 10 to 24 s (sampling the crust). Both exhibit some fast anomalies in the north-eastern part of the model and low perturbations around the RRSZ. The repartition of the velocity perturbations in terms of orientation (NE/SW trend) as well as the location of those anomalies is remarkable.

Lithospheric anomalies

At periods of 24 to 30 s and longer, an E/W dichotomy can be found around the RRSZ, with low velocities in the western part and higher velocities in the eastern part of the model. This is in good agree by receiver function analyses (Nguyen et al. 2013). At periods sampling the upper lithosphere (24 to 30 s), small variations in the fast direction of anisotropy is observed compared to shorter periods, with a small variation in the direction (30°/40°) between the fast axis of the ansitropy on both sides of the RRSZ. This can be explained by frozen anisotropy in the lithosphere beneath the region. At longer periods (40 to 50 s), sampling the lithosphere, the small-scale anomalies seem to merge together and display less heterogeneities than at shorter periods (Figure 11e,f).

One of the dominating features in the isotropic part of our model is the high velocity beneath the South China Block in northeastern part of our model. This anomaly persists up to periods around 40 to 50 s, where the general anisotropic pattern is slightly different than in the crust. Almost no anisotropy is found in the eastern part of the model, with amplitudes smaller than 0.5%, whereas amplitudes of 1% to 1.5% are found in the western part of the region.

Conclusions

In this study, we have constructed anisotropic Rayleigh-wave phase-velocity maps for northern Vietnam using broadband seismograms from the portable broadband seismic network in Vietnam. The models we obtain from Rayleigh waves of different periods reveal features changing both laterally and with period (i.e., reflecting shear-wave speed changes with depth). These variations are linked with the tectonic provinces observed at the surface,

such as that between the Indo-China Block and the South China Block. At short periods, we also observe a clear E/W dichotomy in the studied region which we interpret as a step-like change in the Moho depth, consistent with the results of previous observations. The isotropic part of the model reveals clear differences in the lithospheric structure of the main units of the region, including not only the large-scale (South China and Indo-China Blocks) but also the smaller scale units within them (Simao Block), defining their deep geometry. Lateral and vertical variations of azimuthal anisotropy provide more details on the tectonic evolution and current crustal and lithospheric dynamics beneath the region.

Competing interests
The authors declare that they have no competing interests.

Authors' contributions
CL conceived of the study, performed the measurements and inversions, and wrote the manuscript. ZL has been involved in drafting the manuscript and revising it critically for important intellectual content. BSH and WGH have made substantial contributions to the acquisition of data and helped to draft the manuscript. All authors read and approved the final manuscript.

Acknowledgements
Constructive reviews from two anonymous reviewers and Martha K. Savage (Editor) significantly improved the manuscript. This work was funded by an Academia Sinica Career Development Award (AS-098-CDA-M02) and the National Science Council of Taiwan under grants NSC101-2116-M-001-035 and NSC102-2116-M-001-013. We express our appreciation to the staff of the Vietnam Academy of Science and Technology and Academia Sinica for collecting the data used in this study. Figures were generated with Generic Mapping Tools (Wessel and Smith 1995).

Received: 14 August 2014 Accepted: 26 January 2015
Published online: 24 February 2015

References

Avouac J-P, Tapponnier P (1993) Kinematic model of active deformation in central Asia. Geophys Res Lett 20(10):895–898
Bird P (2003) An updated digital model of plate boundaries. Geochem Geophys Geosyst 4(3):1–52
Chung S-L, Lee T-Y, Lo C-H, Wang P-L, Chen C-Y, Yem NT, Hoa TT, Genyao W (1997) Intraplate extension prior to continental extrusion along the Ailao Shan-Red River Shear Zone. Geology 25(4):311–314
Deschamps F, Lebedev S, Meier T, Trampert J (2008) Azimuthal anisotropy of Rayleigh-wave phase velocities in the east-central United States. Geophys J Int 173:827–843
Endrun B, Lebedev S, Meier T, Tirel C, Friederich W (2011) Complex layered deformation within the Aegean crust and mantle revealed by seismic anisotropy. Nat Geosci 4(3):203–207
Huang B-S, Le TS, Liu C-C, Toan DV, Huang W-G, Wu Y-M, Chen Y-G, Chang W-Y (2009) Portable Broadband Seismic Network in Vietnam for investigating tectonic deformation, the Earth's interior, and early-warning systems for earthquakes and tsunamis. J Asian Earth Sci 36(1):110–118
Huang H-H, Xu ZJ, Wu Y-M, Song X, Huang B-S, Nguyen LM (2013) First local seismic tomography for Red River Shear Zone, northern Vietnam: stepwise inversion employing crustal P and Pn waves. Tectonophysics 584(0):230–239
Huang J, Zhao D, Zheng S (2002) Lithospheric structure and its relationship to seismic and volcanic activity in southwest China. J Geophys Res Solid Earth 107(B10):ESE–13
Kennett BLN, Engdahl ER, Buland R (1995) Constraints on seismic velocities in the Earth from traveltimes. Geophys J Int 122(1):108–124
Knapmeyer-Endrun B, Krüger F, Legendre C, Geissler W (2013) Tracing the influence of the Trans-European Suture Zone into the Mantle Transition Zone. Earth Planetary Sci Lett 363(0):73–87
Knopoff L (1972) Observation and inversion of surface-wave dispersion. Tectonophysics 13:497–519
Lebedev S, Van Der Hilst RD (2008) Global upper-mantle tomography with the automated multimode inversion of surface and S-wave forms. Geophys J Int 173(2):505–518
Lebedev S, Meier T, van der Hilst R (2006) Asthenospheric flow and origin of volcanism in the Baikal Rift area. Earth Planetary Sci Lett 249(3):415–424
Legendre CP, Meier T, Lebedev S, Friederich W, Viereck-Götte L (2012) A shear wave velocity model of the European Upper Mantle from automated inversion of seismic shear and surface waveforms. Geophys J Int 191(1):282–304
Legendre CP, Deschamps F, Zhao L, Lebedev S, Chen Q-F (2014) Anisotropic Rayleigh wave phase velocity maps of eastern China. J Geophys Res Solid Earth 119(6):4802–4820
Legendre CP, Chen Q-F, Zhao L (2014) Lithospheric structure beneath the East China Sea revealed by Rayleigh-wave phase velocities. J Asian Earth Sci – 96:213–225
Lei J, Zhao D, Su Y (2009) Insight into the origin of the Tengchong intraplate volcano and seismotectonics in southwest China from local and teleseismic data. J Geophys Res Solid Earth (1978–2012) 114(B5):B05302
Meier T, Dietrich K, Stöckhert B, Harjes H-P (2004) One-dimensional models of shear wave velocity for the eastern Mediterranean obtained from the inversion of Rayleigh wave phase velocities and tectonic implications. Geophys J Int 156:45–58
Montagner J-P, Tanimoto T (1991) Global Upper Mantle tomography of seismic velocities and anisotropies. J Geophys Res 962:20337–20351
Nguyen LM, Lin T-L, Wu Y-M, Huang B-S, Chang C-H, Huang W-G, Le TS, Nguyen QC, Dinh VT (2012) The first Peak Ground Motion attenuation relationships for north of Vietnam. J Asian Earth Sci 43(1):241–253
Nguyen V-D, Huang B-S, Le T-S, Dinh V-T, Zhu L, Wen K-L (2013) Constraints on the crustal structure of northern Vietnam based on analysis of teleseismic converted waves. Tectonophysics 601(0):87–97
Paige CC, Saunders MA (1982) LSQR: an algorithm for sparse linear equations and sparse least squares ACM Trans Math Softw 8:43–71
Pailoplee S, Choowong M (2014) Earthquake frequency-magnitude distribution and fractal dimension in mainland Southeast Asia. Earth Planets Space 66(8):1–10
Sato Y (1955) Analysis of dispersed surface waves by means of Fourier transform I. Bull Earthquake Res Tokyo Univ 33(1):33–48
Searle M (2006) Role of the Red River Shear Zone, Yunnan and Vietnam, in the continental extrusion of SE Asia. J Geological Soc 163(6):1025–1036
Tapponnier P, Peltzer G, Armijo R (1986) On the mechanics of the collision between India and Asia. Geological Soc Lond Special Publ 19(1):113–157
Trampert J, Woodhouse JH (2003) Global anisotropic phase velocity maps for fundamental mode surface waves between 40 and 150 s. Geophys J Int 154(1):154–165
Wang C-Y, Chan WW, Mooney WD (2003) Three-dimensional velocity structure of Crust and Upper Mantle in southwestern China and its tectonic implications. J Geophys Res Solid Earth 108(B9):2156–2202
Wang J-H, Yin A, Harrison T, Grove M, Zhang Y-Q, Xie G-H (2001) A tectonic model for Cenozoic igneous activities in the eastern Indo-Asian collision zone. Earth Planetary Sci Lett 188(1):123–133
Wang Z, Dahlen FA (1995) Spherical-spline parameterization of three-dimensional Earth models. Geophys Res Lett 22(22):3099–3102
Wessel P, Smith WH (1995) New version of the Generic Mapping Tools. Eos Trans AGU 76(33):329
Wu H-H, Tsai Y-B, Lee T-Y, Lo C-H, Hsieh C-H, Toan D (2004) 3-D shear wave velocity structure of the Crust and Upper Mantle in South China Sea and its surrounding regions by surface wave dispersion analysis. Mar Geophys Res 25(1-2):5–27
Xu Y, Liu J, Liu F, Song H, Hao T, Jiang W (2005) Crust and Upper Mantle structure of the Ailao Shan-Red River Fault zone and adjacent regions. Sci China Series D: Earth Sci 48(2):156–164
Yeh M-W, Lee T-Y, Lo C-H, Chung S-L, Lan C-Y, Anh TT (2008) Structural evolution of the Day Nui Con Voi metamorphic complex: implications on the development of the Red River Shear Zone, northern Vietnam. J Struct Geol 30(12):1540–1553